THE JOURNAL OF PHYSICAL CHEMISTRY B
A JOURNAL OF THE AMERICAN CHEMICAL SOCIETY

pubs.acs.org/JPCB

Article

Capping Layer Determined Self-assembly of Au−Ag Bimetallic Janus Nanoparticles at An Oil/Water Interface by Molecular Dynamics Simulations

Chunlei Zhang, Haihong Jia, Yan-Fang Zhang,* and Shixuan Du*

Cite This: *J. Phys. Chem. B* 2023, 127, 9543−9549

Read Online

ACCESS | Metrics & More | Article Recommendations | Supporting Information

ABSTRACT: Bimetallic Janus nanoparticles (BJNPs) have gained more attention due to their unique catalytic and optical properties. The self-assembly of BJNPs is expected as an effective way to fabricate metamaterials suitable for different potential applications. However, the self-assembly dynamic process of BJNPs, which is key to achieving a controllable synthesis, is limited in both experimental and theoretical investigations. Herein, all-atom molecular dynamics (MD) simulations were employed to investigate the self-assembly process of 1-dodecanethiol (DDT)-decorated Au−Ag BJNPs at an oil−water interface. We demonstrate that DDT's van der Waals (vdW) interaction dominates the self-assembly process. BJNPs form close-packed structures at both fast and slow evaporation rates. Au−Ag BJNPs exhibit relatively larger rotations at a low evaporation rate than those at a high evaporation rate, suggesting that the evaporation rate influences the orientation of the Au−Ag BJNPs. BJNPs tend to orient their electric dipole moments toward the external electric field, according to the *ab initio* MD simulation results. Based on the energy comparison and model analysis, it is found that the parallel array is more stable than the antiparallel one for the Au−Ag BJNP arrays. The dipole−dipole interaction difference between the parallel and antiparallel BJNP arrays obtained according to dipole moment obtained from *ab initio* calculation is qualitatively consistent with that obtained from MD simulations, indicating that the dipole plays a decisive role in determining the orientation of the BJNP array. This work uncovers the self-assembly dynamic process of BJNPs, paving the way for future applications.

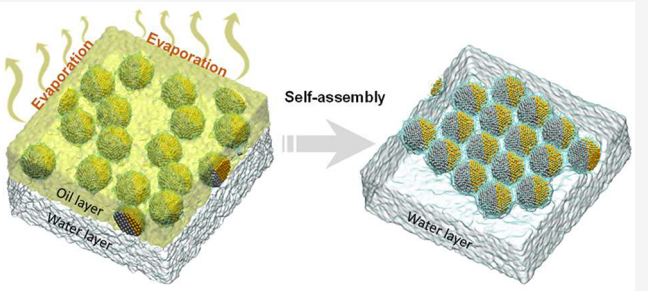

1. INTRODUCTION

Bimetallic nanoparticles (BNPs), with two different metals integrated into a single particle, have broadened the roadmap of nanoparticles. The combination of two metals leads to interesting properties and potential applications compared with homogeneous nanoparticles, which benefit from electronic interactions induced by the versatile compositions and spatial arrangements.[1−4] Based on the atomic spatial distribution, the structures of BNPs are classified into four main categories (Figure S1): alloys or compounds, core−frame, core−shell, and Janus NPs (JNPs).[5,6] Within the family of BNPs, bimetallic Janus nanoparticles (BJNPs) exhibit enhanced catalytic properties and optical properties due to the asymmetrical distribution of metals.[1,7−9] Au−Ag JNP is a representative example. The interaction between the localized surface plasmon resonance of the Au part and that of the Ag part in Au−Ag JNPs induces Fano resonance signals, showing the potential for applications in ultrasensitive chemical or biological sensors. By changing the size of both components and the contact area, the optical property of Au−Ag JNPs can be rationally tuned since it depends on the individual metals and plasmonic coupling in BJNPs.[10]

The self-assembly of NPs provides a simple and powerful way to achieve ordered and well-defined nanoarchitecture.[11−18] These complex NP superstructures with unique and enhanced properties can satisfy advanced technological requirements, such as photovoltaics, energy, and storage devices.[13,18−21] The excellent physicochemical properties of BJNPs make them ideal building blocks self-assembled to form functional nanoarchitecture.[22−24] However, there are rare experimental investigations on the self-assembly dynamics process of BJNPs.[25] In addition, molecular dynamics (MD) simulations are mainly focused on exploring the stability,[26] formation,[27,28] and melting behavior[29] of BJNPs. A physical picture that captures the detailed mechanisms of BJNP self-assembly, which is crucial for precise control in metamaterial synthesis, remains elusive.

Received: July 8, 2023
Revised: October 5, 2023
Accepted: October 9, 2023
Published: October 25, 2023

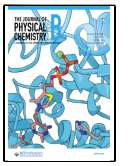

https://doi.org/10.1021/acs.jpcb.3c04600
J. Phys. Chem. B 2023, 127, 9543−9549

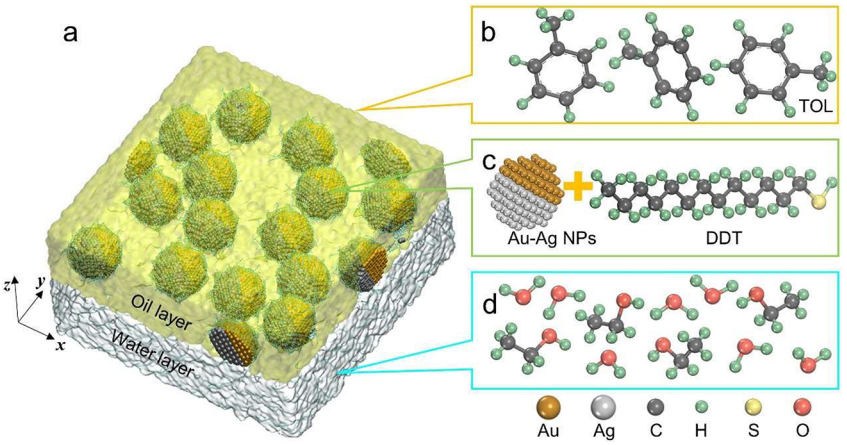

Figure 1. Models of the Au−Ag BJNPs structure. (a) The simulation system consists of the water and oil layers with 16 Au−Ag BJNPs capped by DDT ligands. (b) The oil layer: TOL serving as the solvent. (c) Au−Ag BJNPs with DDT ligands. (d) The water layer: a mixture of ethanol and water.

Herein, we performed all-atom MD simulations to investigate the evaporation-induced self-assembly process of 1-dodecanethiol (DDT)-capped Au−Ag BJNPs at the oil−water interface. By analysis of the interaction energy of different components in DDT-capped NPs, it is found that the van der Waals (vdW) interaction between the capping layers is dominant in the self-assembly process. It is worth noting that a slow evaporation rate gives rise to a notable rotation of Au−Ag BJNPs. Furthermore, the effect of an external electric field on the movement of an Au−Ag BJNP is explored by *ab initio* MD simulation. The results show that the electric dipole moment of the Au−Ag BJNP tends to be consistent with the external electric field. Finally, we designed two ordered, parallel, and antiparallel Au−Ag BJNPs arrays and investigate their structure stability. The antiparallel one is found to be a more stable state, verified by the energy comparison and the analysis of the dipole−dipole interaction models.

2. MODELS AND METHODS

Bimetallic Au−Ag Janus Nanoparticles in the Solvent. Figure 1a presents the initial structure of the whole simulation system consisting of the water layer, oil layer, and 16 Au−Ag BJNPs decorated by capping ligands (DDT). The thicknesses of the toluene and water layers are 10 and 8 nm, respectively (Figure S2). The Au−Ag BJNPs are randomly distributed in the oil layer with TOL molecules serving as the solvent (Figure 1b). 88 DDT molecules attach to every Au−Ag BJNP, improving the stability of BJNPs by saturating dangling bonds (Figure 1c). The water layer is a mixture of ethanol and water (Figure 1d).

Molecular Dynamics Simulation Method. The all-atom MD simulations were performed based on the Gromacs-4.6.7 software package.[30] The intra- and intermolecular interactions of ethanol, DDT, and TOL (toluene) molecules are described by the General AMBER force field. Partial atomic charges for three molecules were obtained from the restrained electrostatic potential (RESP) fitting method.[31,32] We chose the transferable intermolecular potential with 3 points (TIP3P) for water molecules.[33] As for Au and Ag atoms, the interaction was described by the 6−12 Lennard-Jones potential.[34] In the *xy*-plane, we applied the periodic boundary condition, and there were two virtual walls in the *z*-direction.

The force-field for the interaction of walls/surfaces (parallel to the *xy*-plane) with the rest of the system is described by the 9−3 Steele potential, which is expressed in the following formula:[35]

$$V_s(z) = \frac{2\pi\rho_s\varepsilon_{ms}\sigma_{ms}^3}{3}\left\{\frac{2}{15}\left(\frac{\sigma_{ms}}{z}\right)^9 - \left(\frac{\sigma_{ms}}{z}\right)^3\right\}$$

where ρ_s is the number density of the atoms for each wall and z is the distance between atoms in the system and the wall. (σ_s, ε_s) and (σ_m, ε_m) are parameters of Lennard-Jones potential for the wall and the rest of the system (e.g., BJNPs, water molecules, ethanol molecules, and toluene molecules), respectively. Here, we use the values of σ_s = 0.3 nm, ε_s = 0.8 kJ/mol, and $\rho_s = 125/\pi$ nm^{-3}, which are reported in previous ref 36, in the MD simulation. The combination rules, $\sigma_{ms} = (\sigma_m + \sigma_s)/2$ and $\varepsilon_{ms} = (\varepsilon_m\varepsilon_s)^{1/2}$, were used to describe the Lennard-Jones interaction between BJNPs, water molecules, ethanol molecules, toluene molecules, and the wall.

The temperature and pressure were controlled by the thermostat and barostat, respectively.[37] The time step was set as 1 fs; the cutoff distance for short electrostatic interactions and van der Waals were set as 12 Å. As for long-range electrostatic interactions, it was calculated by the particle mesh Ewald (PME) method.

The whole simulated system consists of a water layer and an oil layer. The water layer is a mixture of ethanol and water, and the oil layer includes the TOL molecules as the solvent and 16 spherical Au−Ag BJNPs with DDT capping ligands, in which the diameter of the BJNPs is about 4 nm.

There are 645,908 atoms in the system, including 14,528 Au atoms, 17,232 Ag atoms, 1408 DDT molecules, 3600 ethanol molecules, 12,960 TOL molecules, and 110,812 water molecules. The surface density of the DDT ligands is 0.0175 Å^{-2}, obtained by the following formula:

$$\rho = \frac{N}{S} \approx 0.0175\text{Å}^{-2}$$

where the term ρ is the surface density of DDT ligands; N is the number of DDT molecules on the surface of an Au−Ag BJNP; and S is the surface area of an Au−Ag BJNP surface (Figure S3). After energy minimization, a 50 ns NPT (1 atm, 300 K) MD simulation was performed to equilibrate the

https://doi.org/10.1021/acs.jpcb.3c04600
J. Phys. Chem. B 2023, 127, 9543−9549

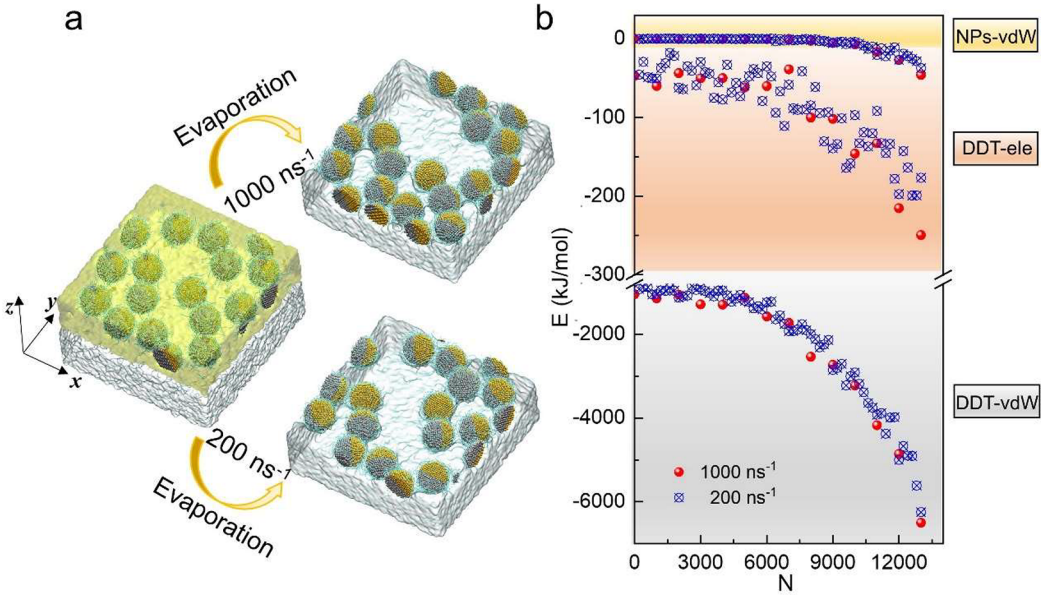

Figure 2. Structures and energy evolution of Au−Ag BJNPs during the self-assembly process. (a) Initial (left panel) and final configurations (right panels) in the self-assembly processes at different evaporation rates of 1000 ns^{-1} and 200 ns^{-1}, respectively. The left panel shows the initial structure with TOL molecules (the yellow part), while the right panels are structures after all the TOL molecules evaporated at different rates. (b) The energy variation as the TOL evaporates at 1000 ns^{-1} (red dots) and 200 ns^{-1} (blue circles). The vertical axis shows the vdW interaction energies between BJNPs ($E_{NPs\text{-}vdW}$, top panel with yellow background), between DDT capping ligands ($E_{DDT\text{-}vdW}$, middle panel with apricot background), and Coulombs interaction between DDT ligands ($E_{DDT\text{-}ele}$, bottom panel with gray background). The lateral axis is the number of TOL molecules evaporated (N).

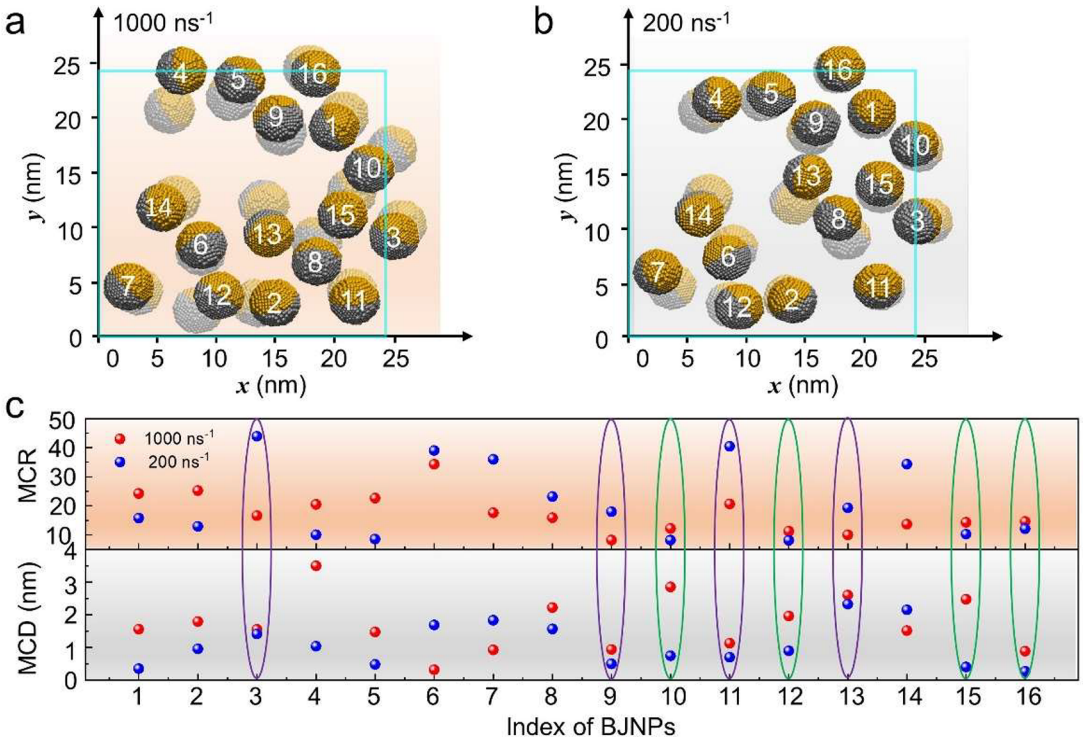

Figure 3. Au−Ag BJNPs and the rotation and in-plane mass-center displacement during the self-assembly process. (a) and (b) Top views of Au−Ag BJNPs before (light-colored balls) and after (dark-colored balls) TOL evaporating with rates of 1000 ns^{-1} and 200 ns^{-1}, respectively. The cyan lines represent the periodic boundary. (c) The variation of rotation angles (upper panel with apricot background) and in-plane mass-center displacements (lower panel with light gray background) of the 16 Au−Ag BJNPs during the self-assembly processes at 1000 ns^{-1} (red dots) and 200 ns^{-1} (blue dots), respectively. The purple (green) ellipses highlight BJNPs with similar displacements (rotation angles).

system before the TOL molecules evaporated. In solvent evaporation, a quasi-equilibrium method was applied by randomly extracting a certain number of solvent molecules from the solution at a predefined time interval, Δt (1 ns) (detailed process shown in Figures S4−9). There were two evaporation rates, with extracting 1000 and 200 TOL

https://doi.org/10.1021/acs.jpcb.3c04600
J. Phys. Chem. B 2023, 127, 9543−9549

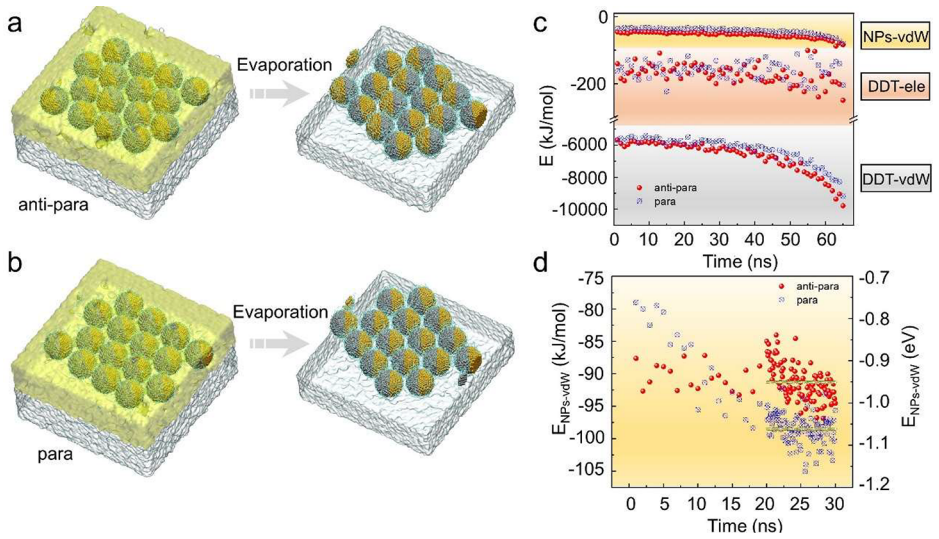

Figure 4. Structures and interaction energies of antiparallel and parallel BJNP arrays before and after the self-assembly process. (a) and (b) Structures of antiparallel (a) and parallel (b) BJNPs before and after evaporation at a rate of 200 ns^{-1}. (c) The energy variation of antiparallel (red dots) and parallel (blue circles) BJNP arrays as the TOL evaporates at a rate of 200 ns^{-1}. The vertical axis shows the vdW interaction energies including $E_{NPs-vdW}$, $E_{DDT-vdW}$, and $E_{DDT-ele}$. The lateral axis is the evaporation time. (d) The variation of $E_{NPs-vdW}$ for antiparallel and parallel BJNPs during the 30 ns NVT equilibrium process.

molecules per nanosecond. Finally, a 30 ns NVT simulation for parallel (antiparallel) structure follows.

Au−Ag BJNP Dipole and *ab initio* MD Simulation with an External Electric Field. Density functional theory (DFT) calculations were performed to calculate the Au−Ag BJNP dipole moment using the Vienna *ab initio* simulation package (VASP) with a plane-wave basis and projector.[38−40] The cutoff energy was 400 eV, and a 1 × 1 × 1 Monkhorst−Pack *k*-points mesh was used in the calculation. The Au−Ag BJNP includes 908 Au atoms and 1077 Ag atoms. The *ab initio* MD simulations were performed at 300 K in an NVT ensemble. The external electric fields (0.1 and 0.05 eV/Å) were applied in the *x*-direction.

3. RESULTS AND DISCUSSION

Structure and Energy Evolution of Au−Ag BJNPs in the Self-assembly Process. Figure 2a gives representative snapshots of the simulation process. The system used for self-assembly goes through an energy minimization, followed by equilibration in the NPT ensemble for an additional 50 ns. The self-assembly process is achieved by evaporating the TOL molecules. Two evaporation rates (1000 and 200 ns^{-1}) are considered here to evaluate the influence on the self-assembly behavior of the Au−Ag BJNPs. The final self-assembly configurations obtained under two different evaporation rates are shown in the right panels of Figure 2a, representing negligible differences. To elucidate the order evolution during the self-assembly process, we categorized Au−Ag BJNPs into three types, unconnected, chain, and packed, as visually represented in Figure S10. The results reveal a notable increase in the population of packed BJNPs as the solvent evaporates (Figure S11), indicating that the system tends to adopt a more ordered structure. The result is consistent with the conclusion in previous work that a two-dimensional triangular (hexagonal) structure should be more stable.[41]

To further understand the self-assembly process, the energy (E) evolution of vdW interactions among BJNPs (NPs-vdW), DDT capping ligands (DDT-vdW), and Coulombs interactions between DDT capping ligands (DDT-ele) is plotted in Figure 2b. As the TOL solvent evaporates, these interaction energies decrease, indicating that a more stable structure gradually forms. It is found that the DDT-vdW interaction energy remains the lowest during the whole evaporation process. In addition, it decreases the fastest among these interaction energies. Thus, the DDT-vdW interaction is dominant during the evaporation process, which determines the motions of BJNPs. It is noteworthy that the variation of these interaction energies at different evaporation rates (1000 and 200 ns^{-1}) roughly overlaps, suggesting that the self-assembly process is insensitive to the evaporation rates.

Au−Ag BJNPs Mass Center Displacement and Rotation. To elucidate the reason the self-assembly process is insensitive to the solvent evaporation rate, we extensively analyzed the change of Au−Ag BJNPs during the self-assembly process. The darker (bottom) and brighter (top) Au−Ag BJNPs (Figures 3a and b) correspond to the structures before and after complete solvent evaporation at evaporation rates of 1000 and 200 ns^{-1}, respectively. BJNPs display apparent displacement in the *xy*-plane and orientation changes after evaporation. However, it is difficult to distinguish the configuration differences of the BJNPs obtained from the two evaporation rates only by comparing the topograph figure.

To clarify the effect of evaporation rates in detail, we analyzed the mass-center rotation (MCR) and in-plane mass-center displacement (MCD) before and after evaporation (Figure 3c). The MCD under 1000 ns^{-1} is generally larger than that under 200 ns^{-1}. The MCDs of BJNPs in green ellipses (numbers 10, 12, 15, and 16) change more dramatically, although they have similar MCRs. Due to the strong DDT-vdW interaction, once the capping ligands on neighboring BJNPs are in contact, it hinders the BJNPs from adjusting their positions. As for the MCR, it shows a relatively larger change at the low evaporation rate of 200 ns^{-1}. In particular, the BJNPs with similar MCDs in the purple ellipses (numbers 3, 9, 11, and 13), have a much higher MCR at a low evaporation rate (200 ns^{-1}). At a low evaporation rate, BJNPs

https://doi.org/10.1021/acs.jpcb.3c04600
J. Phys. Chem. B 2023, 127, 9543−9549

approach each other slowly, generating gradually increased interaction among the DDT capping layers of neighboring BJNPs. Therefore, there is more time for BJNPs to rotate than those at an evaporation rate of 1000 ns^{-1}.

Furthermore, due to the asymmetric spatial structure, the mass center and the geometric center differ, resulting in the net torque and subsequent rotation. Based on the comparison of energy-change behavior under different evaporation rates, self-assembly is insensitive to the evaporation rates. However, structure differences among the BJNPs are evident from MCD and MCR analysis. Thus, adjusting the position and orientation of BJNPs by modifying the solvent evaporation rate proves to be an effective approach for obtaining diverse ordered structures.

Antiparallel (Parallel) Au−Ag BJNPs Arrays Solvent Evaporation Process and Stability. The asymmetric spatial structure of the Au−Ag BJNP gives rise to a dipole oriented perpendicular to the Au−Ag interface. Next, we performed an *ab initio* MD simulation to evaluate the change in the dipole orientation by an external electric field. The results present that the electric dipole moment of the Au−Ag BJNP tends to align with the external electric field (Figures S12−13), suggesting that an external electric field could potentially be employed as a method to control the orientation of the nanoparticles.

Similar to ferromagnetic and antiferromagnetic configurations in magnetic systems, we designed parallel and antiparallel Au−Ag BJNP arrays (Figure 4a) to investigate the stability and differences between the two configurations. The distinct orientations of electric dipole moment in Au−Ag BJNPs are expected to generate alternative ordered superstructures. By iteratively performing the simulation process outlined in Figure 2a, the antiparallel and parallel Au−Ag BJNPs arrays undergo the self-assembly process. Since a two-dimensional hexagonal phase should be the stable phase,[41] here, we used hexagonal-packed BJNP arrays as initial structures. The schematic diagrams of the Au−Ag arrays illustrate that both structures maintain their ordered arrangement throughout the self-assembly process with minimal rotation or detachment of BJNPs, signifying the stability of these structures. Moreover, to quantitively present the interaction energies of NPs-vdW, DDT-ele, and DDT-vdW during the self-assembly process, the corresponding data are plotted in Figure 4b. Notably, the DDT-vdW interaction remains dominant in both antiparallel and parallel structures during the self-assembly process, thereby reinforcing the strong interaction of the DDT capping ligands.

Interestingly, the NPs-vdW, DDT-ele, and DDT-vdW interaction energies of the parallel structure are all higher than those of the antiparallel structure in the self-assembly process. However, the interaction energies keep decreasing during the DDT evaporation process, as shown in Figure 4b (Figure S14), until they go through the following 30 ns NVT equilibrium. Figure 4c depicts the variation of the NPs-vdW interaction energy of the two configurations during the 30 ns NVT equilibrium. The interaction energy eventually converges, indicating that the system arrives at equilibrium. The parallel configuration exhibits a NPs-vdW interaction energy of approximately 0.075 eV lower than that of the antiparallel structure, meaning that the parallel configuration is more stable than the antiparallel one. Considering the Berendsen thermostat may not necessarily generate the canonical ensemble, we performed a 2 ns NVT simulation by employing the Nosé−Hoover thermostat based on the structure obtained after the 30 ns NVT simulation using Berendsen thermostat. The interaction energies ($E_{NPs\text{-}vdW}$) of the antiparallel and parallel BJNP arrays are provided in Figure S15. It is found that the energy of the parallel BJNP array is lower than that of the antiparallel ones, confirming that the parallel BJNP array is more stable than the antiparallel BJNP array.

The NPs-vdW interaction is described by the 12−6 Lennard-Jones potentials without consideration of the electrostatic interaction. The force field parameters for Au and Ag used here are based on experimental results. Therefore, the origin of the energy difference is evaluated by combining the classical dipole−dipole interaction formula as in Figure S16 with first-principles calculations. According to the DFT results, the dipole induced by the asymmetry distribution of Au−Ag is about 13.151 eÅ. Utilizing the formula, the dipole−dipole interactions for the 16 BJNPs in parallel and antiparallel configurations are −0.456 and 0.456 eV, respectively, as shown in Figure S17. The dipole−dipole interaction difference is about 0.912 eV, in agreement with the NPs-vdW interaction energy difference in MD results. This suggests that the orientation of the BJNP array is primarily determined by the dipole−dipole interaction. Besides, it confirms that the parallel configuration is much more stable than the antiparallel configuration. The specific difference in numerical values may arise from temperature effect, the simulation time, and the potential function used to describe the dipole interactions in MD simulations.

4. CONCLUSIONS

In conclusion, the self-assembly process of Au−Ag BJNPs is thoroughly investigated by using the all-atom MD simulation method. The energy change analysis reveals that the DDT-vdW interaction is approximately 1 order of magnitude larger than the NPs-vdW and DDT-ele interactions, making it dominant in the self-assembly process. The solvent evaporation rate has a negligible influence on the change behavior of the interaction energies during self-assembly. However, the MCD and the MCR suggest that a slower evaporation rate is advantageous for the position and orientation adjustment. Additionally, similar to the evaporation rate, applying an external electric field proves to be a feasible strategy for manipulating the self-assembly configuration. The dipole interaction leads to a more stable configuration with parallel Au−Ag BJNPs array compared with the antiparallel one. Therefore, a combination of solvent evaporation and external electric field holds promise as a potential approach for designing ordered orientation super nanocrystal self-assembly BJNPs.

■ ASSOCIATED CONTENT

Supporting Information

The Supporting Information is available free of charge at https://pubs.acs.org/doi/10.1021/acs.jpcb.3c04600.

Schematics of cross sections for four main categories of BNPs; the side view of system including the Au−Ag BJNPs, oil, and water layers; the structure of a Janus particle decorated with the DDT molecules; snapshots of random (antiparallel, parallel) Au−Ag BJNPs assembly; order characterization of Au−Ag BJNPs; the initial structure for *ab initio* MD simulations; structures after 10 ps *ab initio* MD simulations with an external electric field; the antiparallel (parallel) structure energy

https://doi.org/10.1021/acs.jpcb.3c04600
J. Phys. Chem. B 2023, 127, 9543−9549

change of vdW interactions during the evaporation process; the energy change of vdW interaction in antiparallel (parallel) BJNPs under NVT ensemble using Nosé−Hoover thermostat; the schematic of dipole−dipole interaction; the schematic of parallel and antiparallel structure dipoles of BJNPs. (PDF)

AUTHOR INFORMATION

Corresponding Authors

Shixuan Du − *Institute of Physics and University of Chinese Academy of Sciences, Chinese Academy of Sciences, Beijing 100190, China; Songshan Lake Material Laboratory, Dongguan, Guangdong 523808, China;* orcid.org/0000-0001-9323-1307; Email: sxdu@iphy.ac.cn

Yan-Fang Zhang − *Institute of Physics and University of Chinese Academy of Sciences, Chinese Academy of Sciences, Beijing 100190, China*; Email: zhangyanfang@ucas.ac.cn

Authors

Chunlei Zhang − *Institute of Physics and University of Chinese Academy of Sciences, Chinese Academy of Sciences, Beijing 100190, China*

Haihong Jia − *Institute of Physics and University of Chinese Academy of Sciences, Chinese Academy of Sciences, Beijing 100190, China*

Complete contact information is available at: https://pubs.acs.org/10.1021/acs.jpcb.3c04600

Notes

The authors declare no competing financial interest.

ACKNOWLEDGMENTS

This work was supported by grants from the National Natural Science Foundation of China (61888102), the Strategic Priority Research Program of the Chinese Academy of Sciences (XDB30000000), and the Fundamental Research Funds for the Central Universities. MD simulations were carried out on TianHe-1A at the National Supercomputer Center in Tianjin.

REFERENCES

(1) Wang, D.; Li, Y. Bimetallic Nanocrystals: Liquid-Phase Synthesis and Catalytic Applications. *Adv. Mater.* **2011**, *23* (9), 1044−1060.

(2) Lim, B.; Jiang, M.; Camargo, P. H. C.; Cho, E. C.; Tao, J.; Lu, X.; Zhu, Y.; Xia, Y. Pd-Pt Bimetallic Nanodendrites with High Activity for Oxygen Reduction. *Science* **2009**, *324* (5932), 1302−1305.

(3) Gilroy, K. D.; Ruditskiy, A.; Peng, H. C.; Qin, D.; Xia, Y. Bimetallic Nanocrystals: Syntheses, Properties, and Applications. *Chem. Rev.* **2016**, *116* (18), 10414−10472.

(4) Wang, W.; Chiang, T. Y.; Velegol, D.; Mallouk, T. E. Understanding the Efficiency of Autonomous Nano- and Microscale Motors. *J. Am. Chem. Soc.* **2013**, *135* (28), 10557−10565.

(5) Ferrando, R.; Jellinek, J.; Johnston, R. L. Nanoalloys: From Theory to Applications of Alloy Clusters and Nanoparticles. *Chem. Rev.* **2008**, *108* (3), 845−910.

(6) Qiu, J.; Nguyen, Q. N.; Lyu, Z.; Wang, Q.; Xia, Y. Bimetallic Janus Nanocrystals: Syntheses and Applications. *Adv. Mater.* **2022**, *34* (1), No. e2102591.

(7) Song, Y.; Liu, K.; Chen, S. Agau Bimetallic Janus Nanoparticles and Their Electrocatalytic Activity for Oxygen Reduction in Alkaline Media. *Langmuir* **2012**, *28* (49), 17143−17152.

(8) Holmberg, N.; Laasonen, K.; Peljo, P. Charge Distribution and Fermi Level in Bimetallic Nanoparticles. *Phys. Chem. Chem. Phys.* **2016**, *18* (4), 2924−2931.

(9) Zhu, M. J.; Pan, J. B.; Wu, Z. Q.; Gao, X. Y.; Zhao, W.; Xia, X. H.; Xu, J. J.; Chen, H. Y. Electrogenerated Chemiluminescence Imaging of Electrocatalysis at a Single Au-Pt Janus Nanoparticle. *Angew. Chem., Int. Ed. Engl.* **2018**, *57* (15), 4010−4014.

(10) Qiu, J. C.; Xie, M. H.; Lyu, Z. H.; Gilroy, K. D.; Liu, H.; Xia, Y. N. General Approach to the Synthesis of Heterodimers of Metal Nanoparticles through Site-Selected Protection and Growth. *Nano Lett.* **2019**, *19* (9), 6703−6708.

(11) Xu, W. W.; Zhu, B.; Zeng, X. C.; Gao, Y. A Grand Unified Model for Liganded Gold Clusters. *Nat. Commun.* **2016**, *7*, 13574.

(12) Tan, S. F.; Chee, S. W.; Lin, G.; Mirsaidov, U. Direct Observation of Interactions between Nanoparticles and Nanoparticle Self-Assembly in Solution. *Acc. Chem. Res.* **2017**, *50* (6), 1303−1312.

(13) Ma, S.; Yang, D. J.; Ding, S. J.; Liu, J.; Wang, W.; Wu, Z. Y.; Liu, X. D.; Zhou, L.; Wang, Q. Q. Tunable Size Dependence of Quantum Plasmon of Charged Gold Nanoparticles. *Phys. Rev. Lett.* **2021**, *126* (17), No. 173902.

(14) Chen, P.-C.; Liu, X.; Hedrick, J. L.; Xie, Z.; Wang, S.; Lin, Q.-Y.; Hersam, M. C.; Dravid, V. P.; Mirkin, C. A. Polyelemental Nanoparticle Libraries. *Science* **2016**, *352* (6293), 1565−1569.

(15) Feng, J.; Yang, F.; Wang, X.; Lyu, F.; Li, Z.; Yin, Y. Self-Aligned Anisotropic Plasmonic Nanostructures. *Adv. Mater.* **2019**, *31* (19), No. e1900789.

(16) Song, J.; Wu, B.; Zhou, Z.; Zhu, G.; Liu, Y.; Yang, Z.; Lin, L.; Yu, G.; Zhang, F.; Zhang, G.; et al. Double-Layered Plasmonic-Magnetic Vesicles by Self-Assembly of Janus Amphiphilic Gold-Iron(II,III) Oxide Nanoparticles. *Angew. Chem., Int. Ed. Engl.* **2017**, *56* (28), 8110−8114.

(17) Tan, S. F.; Anand, U.; Mirsaidov, U. Interactions and Attachment Pathways between Functionalized Gold Nanorods. *ACS Nano* **2017**, *11* (2), 1633−1640.

(18) Zeng, C.; Chen, Y.; Kirschbaum, K.; Lambright, K. J.; Jin, R. Emergence of Hierarchical Structural Complexities in Nanoparticles and Their Assembly. *Science* **2016**, *354* (6319), 1580−1584.

(19) Lee, S. U.; Hong, J. W.; Choi, S. I.; Han, S. W. Universal Sulfide-Assisted Synthesis of M-Ag Heterodimers (M = Pd, Au, Pt) as Efficient Platforms for Fabricating Metal-Semiconductor Hetero-nanostructures. *J. Am. Chem. Soc.* **2014**, *136* (14), 5221−5224.

(20) Lin, G.; Zhu, X.; Anand, U.; Liu, Q.; Lu, J.; Aabdin, Z.; Su, H.; Mirsaidov, U. Nanodroplet-Mediated Assembly of Platinum Nanoparticle Rings in Solution. *Nano Lett.* **2016**, *16* (2), 1092−1096.

(21) Lin, G.; Chee, S. W.; Raj, S.; Kral, P.; Mirsaidov, U. Linker-Mediated Self-Assembly Dynamics of Charged Nanoparticles. *ACS Nano* **2016**, *10* (8), 7443−7450.

(22) Pankaj, P.; Bhattacharyya, S.; Chatterjee, S. Competition of Core-Shell and Janus Morphology in Bimetallic Nanoparticles: Insights from a Phase-Field Model. *Acta Mater.* **2022**, *233*, No. 117933.

(23) Yin, A. X.; Min, X. Q.; Zhang, Y. W.; Yan, C. H. Shape-Selective Synthesis and Facet-Dependent Enhanced Electrocatalytic Activity and Durability of Monodisperse Sub-10 nm Pt-Pd Tetrahedrons and Cubes. *J. Am. Chem. Soc.* **2011**, *133* (11), 3816−3819.

(24) Zhou, M.; Wang, H.; Vara, M.; Hood, Z. D.; Luo, M.; Yang, T. H.; Bao, S.; Chi, M.; Xiao, P.; Zhang, Y.; et al. Quantitative Analysis of the Reduction Kinetics Responsible for the One-Pot Synthesis of Pd-Pt Bimetallic Nanocrystals with Different Structures. *J. Am. Chem. Soc.* **2016**, *138* (37), 12263−12270.

(25) Long, N. V.; Chien, N. D.; Uchida, M.; Matsubara, T.; Randy, J.; Masayuki, N. Directed and Random Self-Assembly of Pt-Au Nanoparticles. *Mater. Chem. Phys.* **2010**, *124* (2−3), 1193−1197.

(26) Akbarzadeh, H.; Mehrjouei, E.; Ramezanzadeh, S.; Izanloo, C. Ni-Co Bimetallic Nanoparticles with Core-Shell, Alloyed, and Janus Structures Explored by Md Simulation. *J. Mol. Liq.* **2017**, *248*, 1078−1095.

(27) Liang, M.; Xiong, Z.; Hu, Y.; Liu, Y.; Shen, T.; Sun, S.; Zhu, Y. Surface Evolution of Cu-Ag Bimetallic Systems: From Experiments to Molecular Dynamics Simulation. *J. Phys. Chem. C* **2020**, *124* (39), 21829−21842.

(28) Allaire, R. H.; Dhakane, A.; Emery, R.; Ganesh, P.; Rack, P. D.; Kondic, L.; Cummings, L.; Fuentes-Cabrera, M. Surface, Interface, and Temperature Effects on the Phase Separation and Nanoparticle Self Assembly of Bi-Metallic $Ni_{0.5}Ag_{0.5}$: A Molecular Dynamics Study. *Nanomaterials (Basel)* **2019**, *9* (7), 1040.
(29) Akbarzadeh, H.; Mehrjouei, E.; Abbaspour, M.; Shamkhali, A. N. Melting Behavior of Bimetallic and Trimetallic Nanoparticles: A Review of Md Simulation Studies. *Top Curr. Chem. (Cham)* **2021**, *379* (3), 22.
(30) Hess, B.; Kutzner, C.; van der Spoel, D.; Lindahl, E. Gromacs 4: Algorithms for Highly Efficient, Load-Balanced, and Scalable Molecular Simulation. *J. Chem. Theory Comput* **2008**, *4* (3), 435−447.
(31) Bayly, C. I.; Cieplak, P.; Cornell, W. D.; Kollman, P. A. A Well-Behaved Electrostatic Potential Based Method Using Charge Restraints for Deriving Atomic Charges-the Resp Model. *J. Phys. Chem-Us* **1993**, *97* (40), 10269−10280.
(32) Fox, T.; Kollman, P. A. Application of the Resp Methodology in the Parametrization of Organic Solvents. *J. Phys. Chem. B* **1998**, *102* (41), 8070−8079.
(33) Jorgensen, W. L.; Chandrasekhar, J.; Madura, J. D.; Impey, R. W.; Klein, M. L. Comparison of Simple Potential Functions for Simulating Liquid Water. *J. Chem. Phys.* **1983**, *79* (2), 926−935.
(34) Heinz, H.; Vaia, R. A.; Farmer, B. L.; Naik, R. R. Accurate Simulation of Surfaces and Interfaces of Face-Centered Cubic Metals Using 12−6 and 9−6 Lennard-Jones Potentials. *J. Phys. Chem. C* **2008**, *112* (44), 17281−17290.
(35) Yoneya, M.; Kawasaki, M.; Ando, M. Molecular Dynamics Simulations of Pentacene Thin Films: The Effect of Surface on Polymorph Selection. *J. Mater. Chem.* **2010**, *20* (46), 10397−10402.
(36) Pinilla, C.; Del Popolo, M. G.; Lynden-Bell, R. M.; Kohanoff, J. Structure and Dynamics of a Confined Ionic Liquid. Topics of Relevance to Dye-Sensitized Solar Cells. *J. Phys. Chem. B* **2005**, *109* (38), 17922−17927.
(37) Berendsen, H. J. C.; Postma, J. P. M.; van Gunsteren, W. F.; DiNola, A.; Haak, J. R. Molecular Dynamics with Coupling to an External Bath. *J. Chem. Phys.* **1984**, *81* (8), 3684−3690.
(38) Kresse, G.; Furthmuller, J. Efficiency of *ab initio* Total Energy Calculations for Metals and Semiconductors Using a Plane-Wave Basis Set. *Comput. Mater. Sci.* **1996**, *6* (1), 15−50.
(39) Kresse, G.; Hafner, J. *ab initio* Molecular Dynamics for Liquid Metals. *Phys. Rev. B Condens Matter* **1993**, *47* (1), 558−561.
(40) Kresse, G.; Hafner, J. *ab initio* Molecular Dynamics for Open-Shell Transition Metals. *Phys. Rev. B Condens Matter* **1993**, *48* (17), 13115−13118.
(41) Eslami, H.; Bahri, K.; Muller-Plathe, F. Solid-Liquid and Solid-Solid Phase Diagrams of Self-Assembled Triblock Janus Nanoparticles from Solution. *J. Phys. Chem. C* **2018**, *122* (16), 9235−9244.

https://doi.org/10.1021/acs.jpcb.3c04600
J. Phys. Chem. B 2023, 127, 9543−9549